Correspondence

Analysis of Uplink and Downlink Spatial Channel Reciprocity When Using Asymmetric Transceiver

Peize Zhang ⓘ , *Member, IEEE*, Pekka Kyösti ⓘ , Mar Francis De Guzman ⓘ , *Graduate Student Member, IEEE*, Katsuyuki Haneda ⓘ , *Member, IEEE*, and Aarno Pärssinen ⓘ , *Senior Member, IEEE*

Fig. 1. Diagram of the ABF mmWave massive MIMO system using asymmetric transceiver on the BS side.

Abstract—A novel millimeter-wave massive MIMO system using asymmetric transceiver, i.e., unequal number of transmitting (Tx) and receiving (Rx) radio frequency chains, is expected to maintain the advantages of conventional fully digital beamforming architectures, but partly reduce the implementation cost and power consumption. However, uplink and downlink radio channels may become non-reciprocal due to the different dimensions of Tx-Rx antenna arrays. In this paper, we analyze the reciprocity of radio channels observed by practical antenna patterns with different beamwidths. Two metrics are leveraged to measure spatial channel reciprocity based on 142 GHz outdoor channel measurement data and 28 GHz indoor ray-tracing simulation data. The power angular spectrum reciprocity of uplink and downlink radio channels does not hold when the beam pattern of base station Tx array becomes much narrower than that of Rx array. Meanwhile, it becomes increasingly likely that in the extreme case (e.g., significant beamwidth difference between Tx and Rx beam patterns), pronounced angle reciprocity can still be observed in the sparse channels with less multipath components.

Index Terms—Asymmetric transceiver, spatial channel reciprocity, uplink and downlink channels.

I. INTRODUCTION

Millimeter-wave (mmWave) massive MIMO technology has shown promising results in enabling high-throughput communication [1], [2], and is expected to be widely deployed in real-world environments to boost up the mobile broadband services. Implementation of large-scale antenna arrays can provide sufficient beamforming gains to compensate for the severe path loss in mmWave band. In this context, hybrid beamforming (HBF) has drawn considerable attention to balance flexibility, energy efficiency, and implementation cost trade-offs, while still meeting the required transmission performance compared with analog beamforming and fully digital beamforming (DBF) [3], [4].

A more practical HBF massive MIMO system, i.e., sub- or partially connected HBF architecture, is developed by combining multiple array elements into subarray modules, where each subarray is connected with an independent radio frequency (RF) chain and then forms a beam pointing to specific direction via phase and amplitude control [5], [6], [7], [8]. The number of data streams is upper limited by the number of sub-arrays [3] and each beam only benefits from the gain of the subarray. Coverage or signal outage is the main bottleneck in mmWave networks, however, such architecture cannot achieve the full array gain. In addition, HBF design becomes more challenging with increasing the number of antenna elements in terms of the HBF optimization problem and computational complexity especially when considering several practical constraints on RF components, e.g., phase shifters and variable gain amplifiers. Channel estimation for HBF massive MIMO systems generally require heavier beam training overhead compared with the DBF systems.

Despite the current global 5G mmWave rollout adopting HBF architectures, it becomes increasingly likely that conventional DBF architectures (one dedicated RF chain per antenna element) will come true for mmWave communications once the manufacturing cost and power consumption of RF devices dramatically reduced in the near future [6], [7], [8], [9]. In order to maintain the key advantages of fully DBF architecture (e.g., improved dynamic range, flexible beam management, and enhanced transmission capacity) and somewhat reduce its hardware cost, e.g., using less number of analog-to-digital converters (ADCs) than digital-to-analog converters (DACs), an asymmetric DBF (ABF) architecture was discussed in [2], [10]. As shown in Fig. 1, the base station (BS) is equipped with fully DBF arrays and the number of transmitting (Tx) channels for downlink transmission is much larger than that of receiving (Rx) channels for uplink reception. For an ordinal array with isotropic radiators placed at a uniform spacing of half wavelength, the array gain and effective isotropic radiated power (EIRP) are directly proportional to the number of antenna elements. Thus, increasing the number of radiating elements could produce a high-directive radiation pattern together with high-resolution beam steering. In Fig. 1, the BS downlink Tx beam is much narrower than uplink Rx beam. On the user equipment (UE) side, DBF is also employed where transceiver can be either symmetric or asymmetric.

Even though the asymmetric transceiver is employed on the BS side, the conventional DBF scheme is followed for each separate uplink or downlink. Compared with the HBF systems, ABF system inherits the advantages of DBF, which provides more beams with higher beamforming gain and supports wide-angle beam scanning. The BS can get rid of complicated beam management protocols especially in high mobility scenarios, while the system is still available to maintain a sufficient power level for uplink reception [11]. Moreover, the 5G/6G wireless communication systems promise to support various emerging applications, making the uplink/downlink traffic asymmetry more and more pronounced, e.g., much higher downlink data rate and spectral efficiency than uplink [12]. Fortunately, such ABF system could optimize the resource utilization depending on the traffic demand. Compared with the symmetric DBF systems, the ABF system using less Rx RF chains enables to lower the amount of Rx data for real-time massive MIMO baseband processing, as well as the design complexity of RF front-ends and ADCs, leading to the reduction of hardware costs and power consumption. An ABF system operating at 3.5 GHz with 64-Tx and 16-Rx channels has been developed in [13] and the mmWave implementation is already on the way [2].

Radio channel consists of propagation channel, antennas, and radio front-ends, where the wireless system actually operates in the radio channel observed via antennas. Due to the use of asymmetric BS Tx and Rx beams for downlink transmission and uplink reception, respectively, we would have to raise the question of whether the radio channel reciprocity still holds. For example, low-complexity solutions can be exploited to infer downlink channel state information (CSI) based on reconstructed uplink channel if uplink and downlink radio channel reciprocity still holds to some extent, which makes the proposed ABF system more competitive compared with traditional symmetric DBF systems. This motivates us in this paper to investigate the spatial reciprocity of uplink and downlink radio channels and provide some prior knowledge about the impact of beamwidth and channel conditions on radio channel reciprocity from field measurement and ray-tracing simulation data so that the antenna patterns of asymmetric transceivers can be properly designed for different deployment environments. Firstly, two metrics are proposed to evaluate the reciprocity of power angular spectra (PASs) and potential beam directions of uplink and downlink radio channels, respectively. Secondly, the statistical analysis of uplink and downlink radio channel reciprocity is performed based on propagation channel data from 142 GHz outdoor measurement and 28 GHz indoor ray-tracing simulation. Finally, we discuss the impact of using beam patterns with different half-power beamwidths (HPBWs) and channel condition on radio channel reciprocity to draw insights on ABF system design.

II. UPLINK AND DOWNLINK RADIO CHANNEL (NON-)RECIPROCITY

For traditional symmetric systems in the time division duplexing (TDD) mode of operation, reciprocity of uplink and downlink channels is an essential prerequisite for directly applying the estimated uplink CSI in downlink transmission [14]. For example, the uplink and downlink channel matrices of the symmetric DBF system are $\mathbf{H}_{\mathrm{UL}} \in \mathbb{C}^{N \times M}$ and $\mathbf{H}_{\mathrm{DL}} \in \mathbb{C}^{M \times N}$, respectively, where M and N denote the numbers of antenna elements on the UE and BS sides, respectively. Then the reciprocity in the strict sense would mean $\mathbf{H}_{\mathrm{UL}} = \mathbf{H}_{\mathrm{DL}}^{\mathrm{T}}$ within the coherence bandwidth and coherence time. Radio channel non-reciprocity considered in existing works is mainly due to non-identical behavior of the individual Tx and Rx analog radio front-ends [15]. In the frequency division duplexing (FDD) massive MIMO systems, despite instantaneous channel transfer functions cannot be reused directly,

downlink CSI could still be inferred in virtue of the channel reciprocity regarding PASs and path directions [16], [17]. There is a lack of analysis that focuses on radio channel non-reciprocity caused by using non-reciprocal Tx/Rx arrays. With an exception as reported in [18], only partial reciprocity holds in angle-domain channel for the TDD-based massive MIMO system with unequal number of Tx and Rx antennas on the UE side.

For the ABF system shown in Fig. 1, propagation channel is always reciprocal in all practical scenarios, however, radio channel observed by different TX and Rx antenna arrays may become non-reciprocal. First, the dimensions of the uplink and downlink channel matrices are unequal; and second, the radio channels observed via different antenna arrays may be different owning to the improvement of angular resolution. To recover the downlink channel $\mathbf{H}_{\mathrm{DL}} \in \mathbb{C}^{M \times N_{\mathrm{Tx}}}$ based on estimated $\mathbf{H}_{\mathrm{UL}} \in \mathbb{C}^{N_{\mathrm{Rx}} \times M}$, $N_{\mathrm{Rx}} < N_{\mathrm{Tx}}$ with uplink pilots, several uplink-to-downlink channel transfer algorithms has been proposed [11], [19]. The performance of these algorithms mainly depends on the level of spatial channel reciprocity, which is related to Tx/Rx antenna topology and propagation scenario. For example, if uplink and downlink channel reciprocity still holds for specific Tx-Rx array combination and scenario, low-complexity algorithm and antenna selection method will be able to benefit from such reciprocity to support accurate recovery of downlink channel information. Thus, the question arises how link equivalence (especially the spatial channel information) can be profitably exploited to reconstruct downlink CSI with the aid of estimated uplink CSI.

In view of the dearth of metrics to evaluate the spatial channel reciprocity, here we can define reciprocity based on the similarity of power angular distribution observable on, e.g., the BS side. For example, if the power observable through the BS Rx array and RF chains P_{UL} approximates to the power observable by the BS Tx array and RF chains P_{DL} in angle of ϕ, i.e., $P_{\mathrm{UL}}(\phi) \approx P_{\mathrm{DL}}(\phi)$, the uplink and downlink channels are roughly reciprocal. In [20], we proposed two multi-band spatial channel similarity measures by comparing normalized PASs and beam directions, respectively, which could be further extended to characterize PAS and angle reciprocity. For example, uplink and downlink radio channels can be formed by filtering the same propagation channel with Tx and Rx beam patterns of different HPBWs. The higher the similarity level between two beamformed channels, the more pronounced reciprocity between uplink and downlink channels. The channel reciprocity is expected to be related to the beamwidth difference between Tx and Rx beams, as well as the channel conditions, e.g., rich-scattering and sparse channels.

III. CHANNEL DATA COLLECTION AND POST-PROCESSING

A. Outdoor Channel Measurement Campaign

The 142 GHz channel data measured by Aalto university in a city center available in [21] is used for the characterization of channel non-reciprocity. The measurement campaign was conducted with a vector network analyzer based channel sounder, while the impulse response of the sounder obtained via back-to-back measurement was de-embedded during the pre-processing of the measured channel impulse responses (CIRs) [22]. An omni-directional bicone antenna with 45° elevation HPBW was fixed on the Tx side. On the Rx side, directional scanning sounding method was performed [23], where a horn antenna with 10° azimuth HPBW and 40° elevation HPBW was rotated in the azimuth plane in a small step of 5° to capture directional CIRs, while its main lobe was fixed at the horizontal plane. The Tx and Rx antennas were both mounted at the height of 1.85 m above the ground. The radiation patterns

of the bicone and horn antennas were de-embedded from measurement results.

Three Rx locations were selected at the building corners and several Tx locations were distributed along the main street, resulting in a total of 12 line-of-sight (LOS) and 23 non-LOS (NLOS) links with the maximum transmitter-receiver (T-R) separation distance up to 178 m. More details about the Tx and Rx deployments are described in [21]. Using a measurement-based ray-launcher [22], double-directional channel data can be further estimated based on measured single-directional data.

B. Indoor Point Cloud Ray-Tracing Simulation

The 28 GHz indoor channel data in the check-in area of Helsinki-Vantaa airport terminal 2 was obtained via point cloud ray-tracing simulation [24]. The point cloud used in ray-tracing simulation was refined by removing the ceiling and floor of the airport terminal, as well as human blockers. More details about the simulation environment can be found in [25]. Two Tx locations were selected in a side corridor and behind the stairs, respectively. Two kinds of Rx regions were respectively selected for two Tx locations, where Rx locations were distributed in the check-in area but not fully uniform since we excluded Rx locations existing LOS path. A total of 2875 links, composed of 1473 T1-R1 links and 1402 T2-R2 links, is contained in our analysis with the T-R link distances ranging from 5 m to 70 m. Note that only NLOS Rx locations were considered, where LOS paths were obstructed by physical objects. The output of ray-tracing simulator includes the power, delay, and angular information for each path. Note that only 25 strongest paths for each T-R location pair are recorded in the data sheet.

C. Data Post-Processing

Both channel measurement and ray-tracing simulation data share the same data structure, where the l-th propagation path is characterized by a set of channel parameters $\{p_l, \tau_l, \phi_l, \theta_l\}$, including its received power p_l, propagation delay τ_l, azimuth angle of arrival (AOA) ϕ_l, and zenith angle of arrival (ZOA) θ_l. Note that the channel parameters used here have already de-embedded antenna patterns. As the asymmetric transceiver architecture is only employed at the Rx side, the power delay angular profile (PDAP) $P(\tau, \phi, \theta)$ with respect to the direction of arrival can be written as

$$P(\tau, \phi, \theta) = \sum_{l=1}^{L} p_l \delta(\tau - \tau_l) \cdot \delta(\phi - \phi_l) \cdot \delta(\theta - \theta_l), \quad (1)$$

where L is the total number of multipath components (MPCs). If only azimuth beamforming is conducted, PAS with respect to azimuth plane can be synthesized as

$$P(\phi) = \sum_{\tau} \sum_{\theta} P(\tau, \phi, \theta). \quad (2)$$

Note that the antenna effect has been deembedded for both data sets and the $P(\phi)$ only characterizes the spatial power distribution of propagation channel.

The beamforming impact on the characterization of radio channels can be expressed as the circular convolution of an antenna beam pattern $G(\phi)$ and a PAS $P(\phi)$ of propagation channel:

$$\hat{P}(\phi) = \int P(\varphi) G(\phi - \varphi) \, d\varphi. \quad (3)$$

This corresponds to steering the beam pattern to a direction ϕ and collecting the sum power from all observable MPCs weighted with the corresponding beam gains. The $\hat{P}(\phi)$ represents the PAS of radio channel, so-called as beamformed PAS. Here beam patterns of
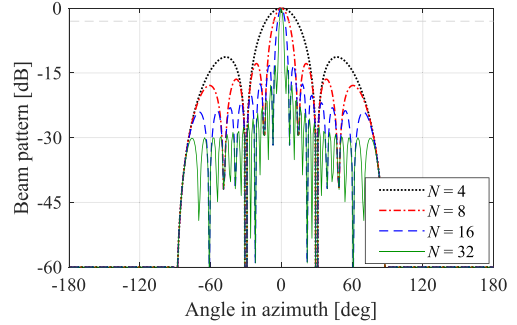

Fig. 2.   Beam patterns of ULAs with 4, 8, 16, and 32 elements.

half-wavelength-spaced uniform linear arrays (ULAs) with different numbers of elements N are used as shown in Fig. 2. The normalized array factor of ULA with isotropic radiators is written as

$$G(\phi, \phi_0) = \frac{\sin\left(\frac{N\pi d}{\lambda}\left[\sin\phi - \sin\phi_0\right]\right)}{N\sin\left(\frac{\pi d}{\lambda}\left[\sin\phi - \sin\phi_0\right]\right)}, \quad (4)$$

where λ is the wavelength, d is the inter-element spacing, and ϕ_0 is the steering angle off boresight. From (4), we can deduce that the beamwidth widens as the beam is scanned away from the boresight. To simplify the analysis, we assume that the beam pattern will not change with beam pointing angle, i.e., using the beam pattern at $\phi_0 = 0°$ in (4). Moreover, the beam patterns of ULAs are defined for $\phi \in [-90°, 90°]$ boresight half plane with all-zero phasing, while the back half plane $\phi \in [-180°, -90°] \vee [90°, 180°]$ is set to a constant -60 dB gain.

In this paper, we only consider the ABF architecture employed on the BS side while keeping the symmetric architecture on the UE side. Here, N_{Tx} and N_{Rx} denote the numbers of antenna elements used for BS downlink transmission and uplink reception, respectively. For symmetric systems, N_{Rx} is equal to N_{Tx}, while $N_{\text{Rx}} < N_{\text{Tx}}$ for asymmetric systems. Here we only change the number of active elements in the ULAs for downlink transmission and uplink reception without changing the inter-element spacing, corresponding to the successive antenna selection scheme. We set N_{Rx} as 4 or 8, which is a typical number of elements in azimuth for commercial phased sub-array based mmWave multibeam systems. The N_{Tx} is set as 8, 16, or 32 for the comparison of beamwidth impact on channel reciprocity. Moreover, different antenna selection schemes can be used with larger or non-uniform spacing of antenna elements depending on design requirements and hardware constraints, leading to changes in HPBW and sidelobe level of beam patterns. We can further evaluate their impacts on the spatial reciprocity of uplink and downlink radio channels using the metrics proposed in this paper.

We give an example of beamformed PAS $\hat{P}(\phi)$ for an indoor simulation link in Fig. 3, where the black circles represent MPCs collected from ray-tracing simulation, i.e., the $P(\phi)$ of propagation channel in (2), and the black doted curve and green solid curve represent the beamformed PASs from (3) using the beam patterns of 4- and 32-element ULAs, respectively. Pronounced channel inconsistency in the beamformed PASs can be observed owning to using different Tx and Rx beam patterns in ABF system.

IV. ANALYSIS, RESULTS, AND DISCUSSION

A. Reciprocity of Beamformed PASs

When we would like to reconstruct channel matrix for downlink transmission, the estimated uplink channel information can be directly reused and expanded only if both links exhibit pronounced reciprocity

TABLE I
STATISTICS OF PSP AND POWER RATIOS R FOR MEASURED AND SIMULATION CASES USING DIFFERENT ULA CONFIGURATIONS

(N_{Tx}, N_{Rx})		(8, 4)		(16, 4)		(32, 4)		(16, 8)		(32, 8)	
$\phi_{3dB,Rx}/\phi_{3dB,Tx}$		2.05		4.16		8.73		2.03		4.27	
Data source[a]		Meas.	Sim.	Meas.	Sim.	Meas.	Sim.	Meas.	Sim.	Meas.	Sim.
PSP [%]	10%	68.7 / 69.5	67.5	45.5 / 45.7	43.8	29.8 / 28.6	28.3	69.1 / 68.5	67.6	45.8 / 45.2	44.2
	50%	70.9 / 71.7	68.4	48.0 / 50.5	45.5	32.9 / 34.9	30.3	70.5 / 71.0	68.5	47.8 / 48.9	45.7
	90%	80.9 / 76.2	77.6	58.0 / 59.2	58.3	40.2 / 38.9	42.5	73.5 / 75.2	76.3	53.3 / 56.0	56.8
$-R$ [dB]	10%	2.54 / 1.01	1.19	4.64 / 2.66	3.11	15.76 / 4.57	6.34	2.01 / 0.70	0.81	2.74 / 1.91	2.42
	50%	0.44 / 0.03	0	0.97 / 0.23	0	2.43 / 1.11	0	0.09 / 0.01	0	0.40 / 0	0
	90%	0.01 / 0	0	0.03 / 0	0	0.12 / 0	0	0 / 0	0	0 / 0	0

[a] For the measurement case, the values in the left and right sides of "·/·" are extracted in LOS and NLOS scenarios, respectively. For the ray-tracing simulation case, only the results in NLOS scenario are considered.
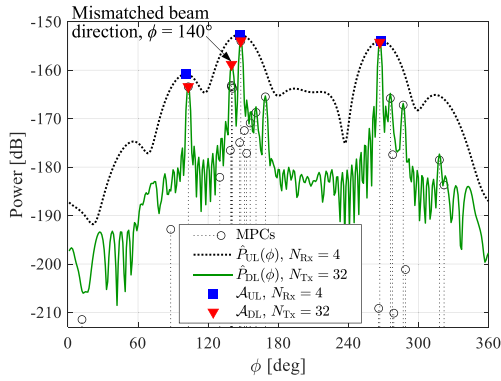

Fig. 3. Example of beamformed PAS $\hat{P}(\phi)$ calculated based on $P(\phi)$ of propagation channel.
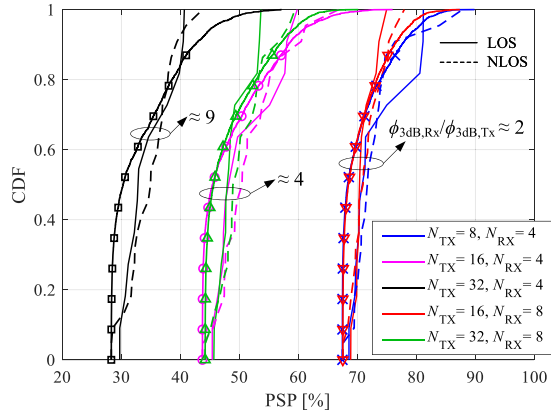

Fig. 4. CDFs of PSP for outdoor measurement case (without markers) and indoor ray-tracing simulation case (with markers).

of beamformed PASs. The PAS similarity percentage (PSP) metric developed in [26] calculates the total variation distance between the normalized beamformed PASs as

$$\rho \ [\%] = 1 - \frac{\int \left| \bar{P}_{DL}(\phi) - \bar{P}_{UL}(\phi) \right| \, d\phi}{2}, \tag{5}$$

where $\bar{P}_{DL}(\phi)$ (or $\bar{P}_{UL}(\phi)$) denotes the normalized beamformed PAS of the downlink (or uplink) channel. The larger PSP value, the more obvious uplink and downlink radio channel reciprocity with respect to beamformed PASs.

For each T-R link, we can obtain a dedicated ρ value for further statistical analysis. Fig. 4 shows the cumulative distribution functions (CDFs) of PSP index based on channel sounding data and ray-tracing simulation data, respectively. Their corresponding statistics are summarized in Table I. The PSP is equal to 100% when the identical Tx and Rx ULAs are employed on the assumption of plane-wave incidence. The PSP value seems inversely proportional to the beamwidth ratio of Rx and Tx arrays. Moreover, PSP value determines which low-complexity solutions work well to infer downlink channel information based on reconstructed uplink channel without any additional training cost. Since high PSP value corresponds to more obvious uplink and downlink channel reciprocity, we suggest that the PSP values at 10th percentile and 50th percentile (median value) need to be both larger than a specific level. As shown in Fig. 4, in 50% of cases the PSP values exceed almost 70% for both outdoor and indoor environments with $(N_{Tx}, N_{Rx}) = (8, 4)$ or $(16, 8)$, i.e., the HPBW of Rx beam $\phi_{3\text{-}dB,Rx}$ is around twice wider than $\phi_{3\text{-}dB,Tx}$. Both measured and simulated results show a similar trend that the PSP values decrease with the increase of $\phi_{3\text{-}dB,Rx}/\phi_{3\text{-}dB,Tx}$. Moreover, the PSP values for LOS links are slightly larger than the results for NLOS links with regard to the measurement case, whereas their differences are statistically insignificant.

B. Reciprocity of Beam Pointing Angles

With the purpose of discovering strongest directional links for downlink transmission and uplink reception, beam training protocols offer an alternative solution without explicit channel estimation. Using different Tx/Rx beams potentially results in different beam pointing angles due to different angular resolutions (i.e., HPBWs). In [26], we developed a beam direction-based channel similarity metric, which first estimates the potential beam directions based on the local maximum values of beamformed PASs $\hat{P}_{DL}(\phi)$ and $\hat{P}_{UL}(\phi)$, and then calculates the power ratio of power summation over different steering angle sets observed by non-reciprocal beam patterns as

$$R \ [\text{dB}] = \frac{\sum_{\phi \in \mathcal{A}_{UL}} \hat{P}_{DL}(\phi)}{\sum_{\phi \in \mathcal{A}_{DL}} \hat{P}_{DL}(\phi)}, \tag{6}$$

where $\mathcal{A}_{DL}$ and $\mathcal{A}_{UL}$ denote the azimuth angle sets of potential beam directions estimated from downlink and uplink radio channels, respectively. Different from the normalized beamformed PAS $\bar{P}(\phi)$ used in (5), here we directly use the actual beamformed PAS $\hat{P}(\phi)$ calculated via (3) without power normalization. In Fig. 3, three (blue squares) and four (green downward-pointing triangles) beam directions can be estimated from $\hat{P}_{UL}(\phi)$ and $\hat{P}_{DL}(\phi)$, respectively. Three matched beam directions can be directly found, while one beam direction towards $\phi = 140°$ is detected only from downlink radio channel.
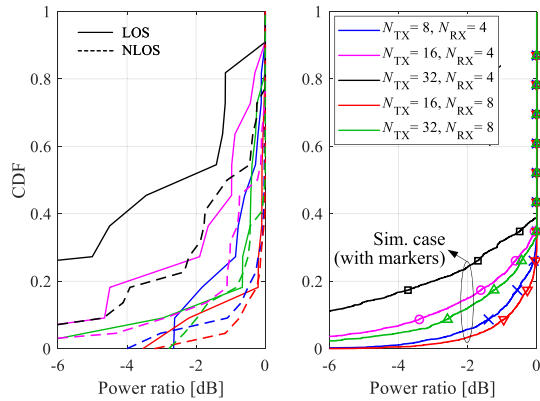
Fig. 5. CDFs of power ratio for outdoor measurement case (without markers) and indoor ray-tracing simulation case (with markers).
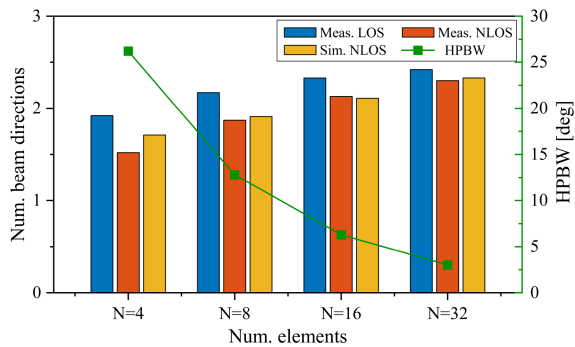

Fig. 6. Comparison of the average number of estimated beam directions across the beamformed channels filtering with different beam patterns.

The power ratio R is less than or equal to 0 dB since more beam directions can be detected from the downlink radio channel observed by narrower beam pattern in comparison with the uplink radio channel observed by wider beam pattern. Considering the beam pointing angles estimated from uplink radio channel are not perfectly matched with those from downlink radio channel which potentially results in significant power degradation, and meanwhile the number of beam directions in uplink channel even become less, we calculate the power ratio via (6) to evaluate the reciprocity of beam pointing angles rather than only comparing the angle difference. The $-R$ represents the power loss introduced by using different Tx and Rx beams. Larger power loss indicates that the angle reciprocity level of uplink and downlink channels will be significantly reduced.

Fig. 5 depicts the CDFs of power ratio for measured and simulated cases. The similar trend can be observed that power ratio R reduces with increase of array size gap. The power loss values for measured case are slightly larger than the simulated results due to more detectable beam directions in outdoor environments. However, in 50% of cases the R values extracted from measurement and simulation data are close to 0 dB with an exception of $(N_{Tx}, N_{Rx}) = (32, 4)$, which is the extreme case with about 8.73-fold increase in the HPBW between small- and large-scale antenna arrays. Thus, angle reciprocity of uplink and downlink radio channel still hold with a focus on beam directions.

In order to analyze the impact of channel condition (e.g., rich scattering or sparse channel) on uplink and downlink channel reciprocity in ABF-based system, we compare the average numbers of estimated beam directions across different scenarios as depicted in Fig. 6. The

PASs of radio channels are observed by different sizes of ULAs, e.g., $N = 4, 8, 16,$ and 32. We can thus derive following conclusions:

1) From Table I, both measured and simulated cases in general show low power loss even when beamwidth difference of Tx and Rx arrays becoming more pronounced. On the contrary to the PAS reciprocity, angle reciprocity of uplink and downlink radio channels still holds in the scenarios with less detectable beam directions.

2) The statistics of power loss $-R$ in different scenarios are related to the average numbers of potential beam directions. For example, more beam directions can be detected for measured LOS links compared with other links. This results in higher power loss, i.e., the reduction of the angle reciprocity, indication that estimated uplink beam direction information cannot be directly reused for downlink transmission.

3) The number of observed beam directions is proportional to the antenna array size. In other words, the increased number of ULA elements leads to narrower beam pattern (see green line in Fig. 6) and higher angular resolution, which enables to detect more beam directions. Increasing beam number difference between non-reciprocal uplink and downlink radio channels generally results in lower power ratio.

V. CONCLUSION

In this paper, we analyze the spatial channel reciprocity in massive MIMO systems when using asymmetric Tx and Rx arrays for downlink transmission and uplink reception, respectively. The PSP and beam direction based metrics are respectively utilized for measuring PAS and angle reciprocity based on 142 GHz outdoor channel sounding data and 28 GHz indoor ray-tracing simulation data. The reciprocity of beamformed PASs only holds when the HPBW of the BS Rx antenna array is not significantly (e.g., no more than twice) wider than that of Tx antenna array. The angle reciprocity is determined not only by the beamwidth difference between the Tx and Rx arrays, but also by the propagation scenario. For the scenario having more scatterers, angle reciprocity becomes more sensitive to the Tx-Rx beamwidth difference. Furthermore, if channel reciprocity still holds to some extent, we can benefit from such reciprocity to exploit low-complexity algorithm and optimize transceiver antenna design for accurate recovery of downlink channel information from estimated uplink channel in the ABF system.

REFERENCES

[1] S. A. Busari, K. M. S. Huq, S. Mumtaz, L. Dai, and J. Rodriguez, "Millimeter-wave massive MIMO communication for future wireless systems: A survey," *IEEE Commun. Surveys Tut.*, vol. 20, no. 2, pp. 836–869, Secondquarter 2018.

[2] W. Hong et al., "The role of millimeter-wave technologies in 5G/6G wireless communications," *IEEE J. Microw.*, vol. 1, no. 1, pp. 101–122, Jan. 2021.

[3] A. F. Molisch et al., "Hybrid beamforming for massive MIMO: A survey," *IEEE Commun. Mag.*, vol. 55, no. 9, pp. 134–141, Sep. 2017.

[4] J. Zhang, X. Yu, and K. B. Letaief, "Hybrid beamforming for 5G and beyond millimeter-wave systems: A holistic view," *IEEE Open J. Commun. Soc.*, vol. 1, pp. 77–91, 2020.

[5] V. Raghavan et al., "Millimeter-wave MIMO prototype: Measurements and experimental results," *IEEE Commun. Mag.*, vol. 56, no. 1, pp. 202–209, Jan. 2018.

[6] X. Gu et al., "Development, implementation, and characterization of a 64-element dual-polarized phased-array antenna module for 28-GHz high-speed data communications," *IEEE Trans. Microw. Theory Tech.*, vol. 67, no. 7, pp. 2975–2984, Jul. 2019.

[7] S. Mondal, L. R. Carley, and J. Paramesh, "Dual-band, two-layer millimeter-wave transceiver for hybrid MIMO systems," *IEEE J. Solid-State Circuits*, vol. 57, no. 2, pp. 339–355, Feb. 2022.

[8] A. Sethi et al., "Chip-to-chip interfaces for large-scale highly configurable mmWave phased arrays," *IEEE J. Solid-State Circuits*, vol. 58, no. 7, pp. 1987–2004, Jul. 2023.

[9] E. Björnson, L. Sanguinetti, H. Wymeersch, J. Hoydis, and T. L. Marzetta, "Massive MIMO is a reality–What is next? Five promising research directions for antenna arrays," *Digit. Signal Process.*, vol. 94, pp. 3–20, Nov. 2019.

[10] W. Hong, J. Zhou, J. Chen, Z. Jiang, C. Yu, and C. Guo, "Asymmetric full-digital beamforming mmWave massive MIMO systems for B5G/6 G wireless communications," in *Proc. IEEE Asia-Pacific Microw. Conf.*, Hong Kong, China, 2020, pp. 31–32.

[11] X. Yang, S. Jin, G. Y. Li, and X. Li, "Asymmetrical uplink and downlink transceivers in massive MIMO systems," *IEEE Trans. Veh. Technol.*, vol. 70, no. 11, pp. 11632–11647, Nov. 2021.

[12] ITU, "Minimum requirements related to technical performance for IMT-2020 radio interface(s)," Tech. Rep. ITU-R M.2410-0, Nov. 2017.

[13] C. Guo et al., "Design and implementation of a full-digital beamforming array with nonreciprocal Tx/Rx beam patterns," *IEEE Antennas Wireless Propag. Lett.*, vol. 19, no. 11, pp. 1978–1982, Nov. 2020.

[14] T. L. Marzetta, E. G. Larsson, H. Yang, and H. Q. Ngo, *Fundamentals of Massive MIMO*. Cambridge, U.K.: Cambridge Univ. Press, 2016.

[15] O. Raeesi, A. Gokceoglu, and M. Valkama, "Estimation and mitigation of channel non-reciprocity in massive MIMO," *IEEE Trans. Signal Process.*, vol. 66, no. 10, pp. 2711–2723, May 2018.

[16] H. Xie, F. Gao, S. Jin, J. Fang, and Y.-C. Liang, "Channel estimation for TDD/FDD massive MIMO systems with channel covariance computing," *IEEE Trans. Wireless Commun.*, vol. 17, no. 6, pp. 4206–4218, Jun. 2018.

[17] Y. Han, Q. Liu, C.-K. Wen, M. Matthaiou, and X. Ma, "Tracking FDD massive MIMO downlink channels by exploiting delay and angular reciprocity," *IEEE J. Sel. Topics Signal Process.*, vol. 13, no. 5, pp. 1062–1076, Sep. 2019.

[18] J. Tan and L. Dai, "Channel feedback in TDD massive MIMO systems with partial reciprocity," *IEEE Trans. Veh. Technol.*, vol. 70, no. 12, pp. 12960–12974, Dec. 2021.

[19] J. Lu, J. Zhang, S. Cai, B. Li, X. Zhu, and W. Hong, "Downlink wideband channel estimation for asymmetrical full-digital system," *IEEE Wireless Commun. Lett.*, vol. 11, no. 9, pp. 1830–1834, Sep. 2022.

[20] P. Zhang, P. Kyösti, K. Haneda, P. Koivumäki, Y. Lyu, and W. Fan, "Out-of-band information aided mmWave/THz beam search: A spatial channel similarity perspective," *IEEE Commun. Mag.*, vol. 62, no. 2, pp. 86–92, Feb. 2024.

[21] M. F. De Guzman, K. Haneda, and P. Kyösti, "Measurement-based MIMO channel model at 140 GHz (V1)," *Zenodo*, Feb. 2023. [Online]. Available: https://zenodo.org/records/7640353

[22] M. F. De Guzman, P. Koivumäki, and K. Haneda, "Double-directional multipath data at 140 GHz derived from measurement-based ray-launcher," in *Proc. IEEE 95th Veh. Technol. Conf.*, Helsinki, Finland, 2022, pp. 1–6.

[23] Y. Xing and T. S. Rappaport, "Millimeter wave and terahertz urban microcell propagation measurements and models," *IEEE Commun. Lett.*, vol. 25, no. 12, pp. 3755–3759, Dec. 2021.

[24] P. Koivumäki, G. Steinböck, and K. Haneda, "Impacts of point cloud modeling on the accuracy of ray-based multipath propagation simulations," *IEEE Trans. Antennas Propag.*, vol. 69, no. 8, pp. 4737–4747, Aug. 2021.

[25] J. Vehmas, J. Järveläinen, S. L. H. Nguyen, R. Naderpour, and K. Haneda, "Millimeter-wave channel characterization at helsinki airport in the 15, 28, and 60 GHz bands," in *Proc. IEEE 84th Veh. Technol. Conf.*, Montreal, QC, Canada, 2016, pp. 1–5.

[26] P. Kyösti, P. Zhang, A. Pärssinen, K. Haneda, P. Koivumäki, and W. Fan, "On the feasibility of out-of-band spatial channel information for millimeter-wave beam search," *IEEE Trans. Antennas Propag.*, vol. 71, no. 5, pp. 4433–4443, May 2023.